MoS_2–Carbon Nanotube Hybrid Material Growth and Gas Sensing

Geetanjali Deokar, Péter Vancsó, Raul Arenal, Florent Ravaux, Juan Casanova-Cháfer, Eduard Llobet,* Anna Makarova, Denis Vyalikh, Claudia Struzzi, Philippe Lambin, Mustapha Jouiad,* and Jean-Francois Colomer*

Hexagonal-shaped nanoplates (HNPs) of MoS_2 on vertically aligned carbon nanotubes (CNTs) over a patterned area (a circular area of 1 cm^2 diameter) are produced by chemical vapor deposition technique. With an optimized initial Mo film thickness, a uniform coverage of MoS_2 HNPs with a thickness around 20 nm is achieved. The results confirm that the CNT template plays an important role in the MoS_2 HNPs growth. Each MoS_2 HNP consists of abundant exposed edges, interesting for sensing and catalysis applications. High crystallinity and quality of the as-produced material are revealed by X-ray photoelectron and Raman spectroscopies. Furthermore, NO_2 gas-sensing studies show better sensitivity and recovery for MoS_2/CNT samples as compared to pristine CNTs. The detection of NO_2 gas in a few tens of parts per million to a few hundreds of parts per billion range, at room temperature, is achieved. Density-functional theory calculation indicates that the exposed edges of MoS_2 play a significant role in the NO_2 sensing as compared to horizontally aligned MoS_2 layers. The present report can promote the research toward the fabrication of efficient and reliable MoS_2-based hybrid materials for toxic gas-sensing applications for air quality monitoring in various environments.

1. Introduction

Unlike the zero band-gap graphene, semiconductor materials[1–4] with reactive sites for redox reactions are particularly interesting for gas sensors. Among the various other possible active materials in gas-sensing devices, carbon nanotubes (CNTs) are good candidates. For more than a decade, quite detailed studies have been devoted to use CNTs for gas-sensing applications.[2] Using CNTs as an NO_2 gas sensor was first proposed by Kong et al.[5] The functionalization of CNTs by organic polymers or catalytic metal nanoparticles was found to be a good strategy to enhance the sensitivity and the selectivity of the CNT-based sensors.[2] Metal functionalized sensors can operate at higher temperatures and in harsh environments, as they are both mechanically and chemically robust and stable, as compared to polymer-based functionalized sensors. It has been shown that the sensitivity of the CNT gas sensor functionalized using metal-nanostructures, depends on nanocluster size and shape.[6] Indeed, the size of the metal clusters is necessary to maximize the effect of the gas adsorption at the corners and edges and so to affect the electron transport in the CNTs by the charge transfer.[6]

In the past few years, it has been emphasized experimentally[7,8] and theoretically[4,9,10] that semiconductive MoS_2 is a potential candidate material for gas-sensing applications. It has been reported that MoS_2 structural defects, including point defects,[11] grain boundaries,[12] and edges[3,13] play significant roles in sensing applications. However, large-scale fabrication of sensors, their selectivity tuning, and noise reduction are still a challenge. Therefore, there is significant scope remained to explore new materials with advanced properties. New materials often generate entirely new possibilities, pushing the limits of the accepted boundaries of material properties within which engineers operate.[14] With the increasing demand of highly sensitive, fast, and stable sensors, a series of sensing applications of nanoscale MoS_2-based composites and hybrids have been of growing interest.[15] Out of various methods for MoS_2based hybrid nanomaterials growth, chemical vapor deposition (CVD) is a promising approach to achieve high-quality MoS_2 nanosheets (NSs) with good control on shape, size and number of horizontally or vertically stacked MoS_2 layers.[16,17]

Here, we present our work on the functionalization of vertically aligned CNTs (va-CNTs) by a growth of MoS_2 hexagonalshaped nanoplate (HNP) and their use for gas sensing. The hybrid material produced using CVD technique was characterized by employing various microscopy and spectroscopy characterization tools. The obtained MoS_2 HNPs consist of highly crystalline structures and have abundant exposed edges, which can be very useful in applications such as sensing,[3] catalysis,[18] Li-ion battery,[19] etc. We have explored the gas (NO_2 and NH_3) sensing

performance for the MoS_2/CNT hybrid system. The hybrid samples containing MoS_2 HNPs with exposed edges exhibit relatively rapid detection of NO_2 as compared to the pristine va-CNT and monolayer MoS_2 making it a potential candidate for sensor device application. The obtained results are discussed based on density-functional theory (DFT) calculation results.

2. Results and Discussion

2.1. Material Characterization

In the present work, patterned growth of MoS_2/CNT hybrid material was achieved. The Mo film with defined thickness (10 to 50 nm) deposited on the va-CNT sample and sulfurized for 60 min at 850 °C resulted in MoS_2 growth on CNTs (refer to the Experimental Section). The morphology of the synthesized material was examined by scanning electron microscope (SEM), and the images are shown in **Figure 1**. The inset of Figure 1a shows a typical patterned (circular area with 1 cm^2 diameter) CNT growth on Si substrate. In Figure 1a,b, cross-section SEM images of the sample are shown where the MoS_2 material can be clearly seen, especially on the top of the CNTs. Furthermore, the plan-view SEM images (Figure 1c,d) show that the synthesized material consists of well-defined HNPs with uniform size. The thickness of the nanoplates is about 20 nm, estimated from standing HNPs. The average length of the HNP along the diagonal of the hexagon is about 200–300 nm, as it can be measured from SEM images, and further confirmed by transmission electron microscopy (TEM) (Figure 3a). Two morph ologies of MoS_2 were observed when Mo film was deposited on the full sample (CNT and Si surface without CNT). On CNT free Si substrate, vertically aligned MoS_2 nanosheet growth was seen as reported previously.[20] By contrast, on the va-CNTs growth of MoS_2 HNPs was noticed. An equilibrium morphology of 2H-MoS_2 has a triangular shape. However, other morpho logies such as nanowires,[21] nanotubes,[22] nanoplates,[23] etc., by changing the growth parameter had been reported previously. In our studies, the CNT template seems to play an important role in the nucleation and growth of MoS_2 HNPs similar in the case of epitaxially grown MoS_2 on graphene substrates where hexagonal MoS_2 flakes have been reported.[24] Selective growth of MoS_2 HNP can be achieved by depositing Mo film on the patterned CNT by putting a mask to cover the bare-Si substrate sample. In further studies, the Si substrate with a mask on CNT free area (during Mo film deposition) was used for MoS_2 growth.

The Raman measurements revealed the growth of 2H-MoS_2 on va-CNTs (**Figure 2**).[25] In micro-Raman spectroscopy, a sample volume with an illuminated area of 0.6 μm can be investigated, which provides clear information on the overall composition of the material in the given volume (for 2–3 μm depth). In the low-energy region, the Raman spectrum of the MoS_2/CNT heterostructure exhibits the two most intense peaks at 376.8 and 402.4 cm^{-1} corresponds to the E^1_{2g} and A_{1g} modes of 2H-MoS_2 (Figure 2). The presence of the sharp peaks indicates a high crystalline nature of the formed MoS_2 deposit. The intensity ratios for E^1_{2g} and A_{1g} peaks are ≈0.63 and ≈0.45 for the MoS_2 HNP and bulk MoS_2, respectively. The frequency difference between E^1_{2g} and A_{1g} modes can be used as a robust and convenient diagnostic of the number of MoS_2 layers.[26,27] The observed difference of 25.6 cm^{-1} indicates that the MoS_2 HNPs consist of five or more MoS_2 layers. Additionally, the presence of Raman modes of first order at 1350 cm^{-1} (D band) and 1580 cm^{-1} (G band) and second order at 2780 cm^{-1} (2D band) corresponding to crystalline multiwalled CNTs was observed.[19]

SEM results for samples of different Mo film thicknesses were treated while keeping the other growth parameters constant is presented in Figure S1 (Supporting Information). We found that the Mo film thickness significantly influences the size and density of HNPs. In the case of a 50 nm sulfurizedMo-film HNP growth with higher density and higher substrate surface (va-CNT top-surface)

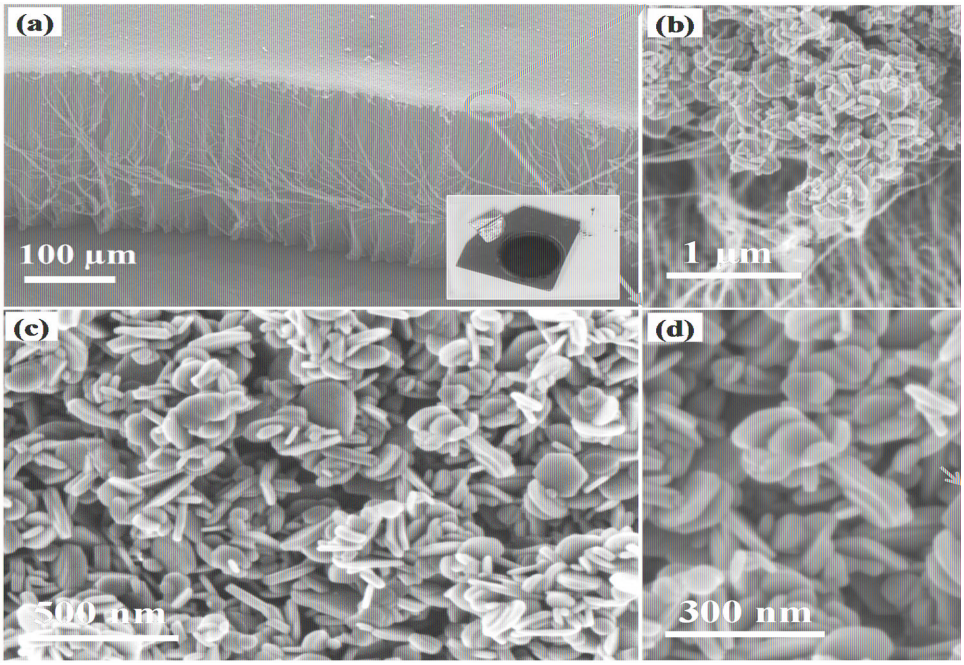

Figure 1. SEM images of MoS_2/CNT sample synthesized by a 50 nm Mo film sulfurized at 850 °C with 420 mg of S powder for 60 min. a,b) Low and high resolution cross-section view SEM images with a typical patterned CNT/Si sample photo in the inset of panel (a). c,d) Surface view SEM images. The typical standing and flat lying HNPs are marked with magenta and orange arrows, respectively.

coverage was observed as compared to that for 25 nm sulfurized-Mo film and 10 nm sulfurized-Mo-film samples. For 10 nm sulfurized-Mo-film sample, a growth of a few large (250 nm) size HNPs was observed. Additionally, the presence of a few tens of nm (10–30 nm) HNPs was observed for the same sample by low-resolution TEM imaging (Figure S2a, Supporting Information). It can be noted that the as-grown HNPs were produced only in a 1 h, as compared to the previously reported lengthy (≥27 h) and two-step method for growth of MoS_2 HNPs by calcination of MoS_2 nanosheets.[23]

Typical TEM observations of as-grown material are presented in **Figure 3**. The nanoplates with hexagonal shape (schematic in the inset of Figure 3a) in agreement with the SEM results (Figure 1c) can be observed from Figure 3a (also, Figure S2a, Supporting Information). The presence of multiwalled CNTs of 5–10 nm outer diameter can be easily noticed from Figure 3a and Figure S2. The relatively dark and thin objects in Figure 3a are standing HNPs. In Figure 3b, the high resolution scanning transmission electron microscopy (HR-STEM) image is taken on standing HNP, where the MoS_2 layers with exposed edges are separated by 0.63 nm. (In the inset the view-plane is highlighted by blue on the schematic of HNP.) The interlayer spacing is slightly higher than the *d*-spacing of the (002) planes of a hexagonal MoS_2 bulk lattice (0.62 nm). Figure 3c shows an HR-TEM image of the flat lying HNP. The HR-TEM image (Figure 3d) over the orange squared area in Figure 3c, indicates that the typical hexagonal pattern of MoS_2 is maintained without any defects in the grain. Moreover, the presence of bright hexagonal spots as it

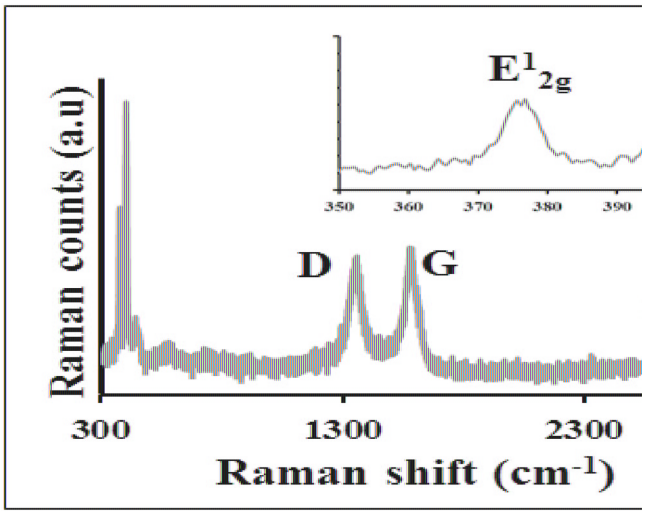

Figure 2. Raman spectra with zoom in over 350–420 cm^{-1} in the inset for MoS_2/CNT sample synthesized by a 50 nm Mo film sulfurized at 850 °C with 420 mg of S powder for 60 min.

can be seen from the fast Fourier transform (FFT) pattern displayed in Figure 3e for the same area indicating good crystalline quality of the NSs. From the TEM imaging analysis, it can be seen that each MoS_2 HNP bearing eight surfaces consists of abundant exposed edges. Such a material with the huge active surface is particularly highly interesting for catalysis and sensing applications.

We have investigated the pristine CNTs and MoS_2/CNT samples using angular-resolved near-edge X-ray absorption fine structure (NEXAFS). **Figure 4** shows the C K-edge spectra of the 10 nm Mo film on CNT sulfurized sample. The angle between the incident photon beam and the sample surface plane was changed between 20° and 90°. The analysis of the angular-dependent C K-edge NEXAFS spectra reveals a reasonable degree of order with an orientation parameter close to that of the pristine CNTs (refer to Figure S3, Supporting Information). The data indicate that the vertical alignment of the CNT is preserved even after the MoS_2 formation on top of them.

Additionally, the MoS_2/CNT hybrid samples chemical composition was analyzed by using X-ray photoelectron spectroscopy (XPS). **Figure 5**a shows the C 1s spectra taken for the pristine CNT sample and for the MoS_2/CNT sample with

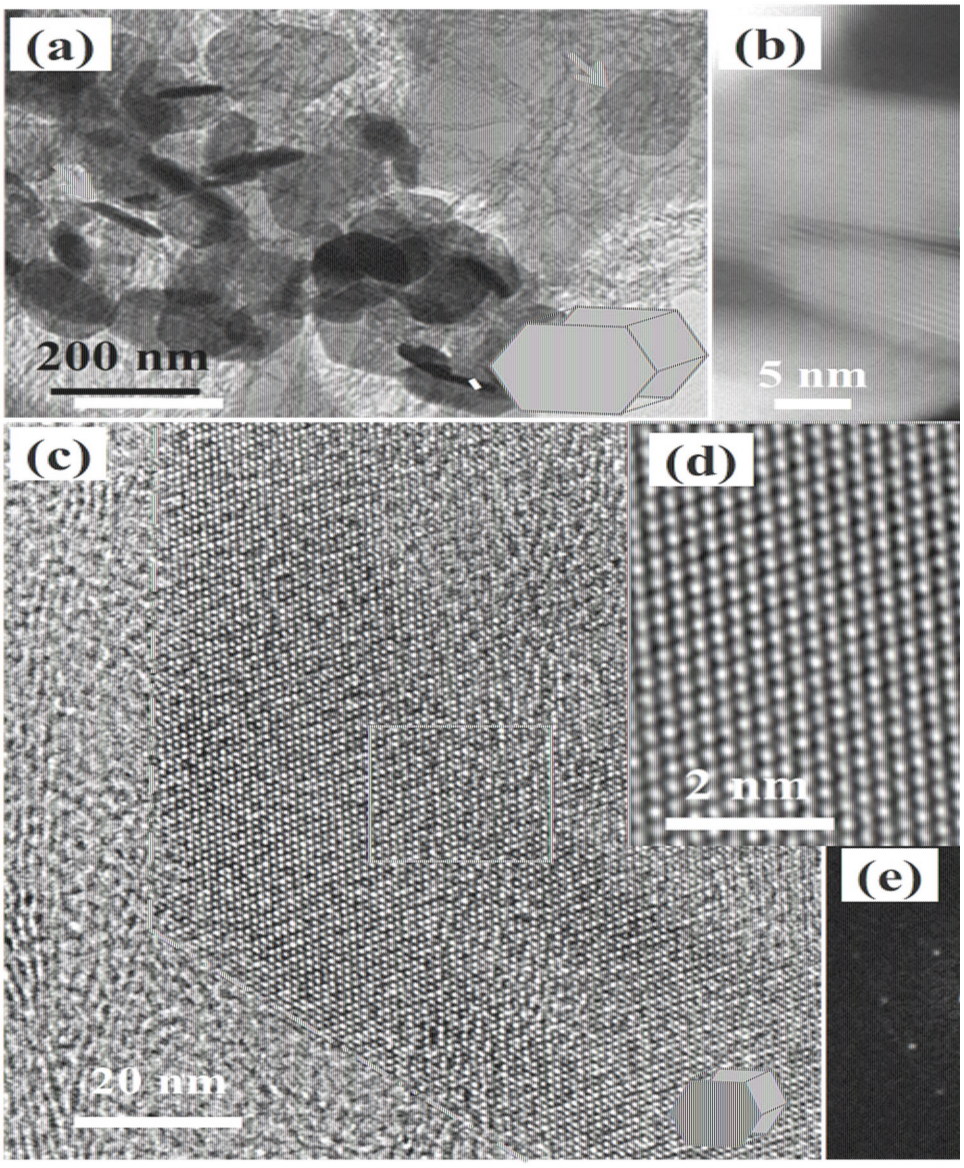

Figure 3. MoS_2/CNT sample synthesized by a 50 nm Mo film sulfurized at 850 °C with 420 mg of S powder for 60 min. a) Low-resolution TEM image of HNPs and CNTs on Cu grid with a schematic of HNP shape in the inset. The standing and flat HNPs are marked with magenta and orange arrows, respectively. b) HR-STEM image of MoS_2 HNP along the edge (view-plane highlighted by blue, on the schematic of HNP in the inset). The typical thickness of 11.3 with (18 MoS_2 layers) nm of the HNPs marked by a magenta arrow. c) HR-TEM images of flat HNP corner (view-plane highlighted by blue on the schematic of HNP in the inset) and its border marked by a yellow line. d) HR-TEM image for the area marked with an orange square in panel (c). e) FFT patterns for the orange squared area marked in panel (c).

25 nm initial Mo film thickness. Both spectra are characterized by a single peak structure, implying that chemical environment of carbon atoms was not dramatically changed upon CNT functionalization. However, lower binding energy shift of 0.1 eV of the hybrid sample spectrum as compared to the pristine CNT implies p-doping of CNTs by MoS_2. In Figure 5b,c, the core level spectra of Mo 3d and S 2s and S 2p are presented for samples with of 10, 25, and 50 nm initial Mo thickness (see Figure S4 of the Supporting Information for data fitting analysis). Since we have not observed Mo oxide and polysulfide (S_n^{2-} and S^{4+}) species in the case of MoS_2/CNT with 50 nm initial Mo film, these samples were used for the gas-sensing studies.

2.2. Gas-Sensing Results

Successive detection and recovery cycles to increasing concentrations of NO_2 and to NH_3 for an MoS_2/CNT sample are shown in **Figure 6**a,b, respectively. While detection is performed at room temperature, the two-step recovery process (see the Experimental Section), including heating at 100 °C, is needed for fully restoring the baseline resistance during the cleaning phase

(Figure S5a, Supporting Information). This is clearly visible for NO_2 in Figure 6a. The heating step was not applied during NH_3 detection (Figure 6b), which resulted in a lack of baseline recovery after the detection cycles. In agreement with

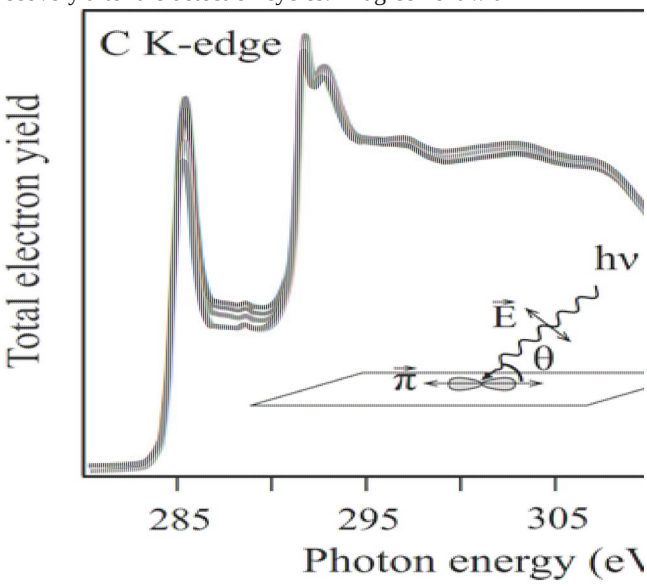

Figure 4. C K-edge NEXAFS spectrum of the MoS_2/CNT hybrid (for 10 nm Mo film on CNT and sulfurized) taken at different angles of incidence. Experimental geometry is shown in the inset.

previous experimental findings,[7] MoS_2–CNT hybrids are also more sensitive to NO_2 than to NH_3 (Figure 6c), which may be attri buted to the different binding energies and charge transfers of the molecules to MoS_2.[9,10] The sensitivity to NO_2 (slope of the calibration curve shown in Figure 6d) is 0.192% × ppm^{-1} in the range from 25 to 100 ppm. The response of the hybrid nanomaterial to lower NO_2 concentrations was also investigated. **Figure 7** shows the responses to 25 and 100 ppb. In this range, the sensitivity is 0.023% × ppb^{-1}. Considering the noise levels, present in the signals (about 1 mΩ) shown in Figure 7 and assuming a signal-to-noise ratio of 3 as required to be properly distinguished a response from the noise, the limit of detection for NO_2 can be estimated to be near 2 ppb.

The MoS_2/CNT system performance for NO_2 sensing was also tested in humidity conditions (Figure S6, Supporting Information).

In the presence of humidity, the response toward 50 ppm of NO_2 significantly increases. It raises from 12.6% under dry conditions to 21% at 30% relative humidity (RH) at 20 °C (Figure S6, Supporting Information). The response further increases to 22.2% when the moisture level reaches 50% RH (20 °C). The change from dry conditions to a moderate humidity level (i.e., 30%) results in a very significant increase in response (1.7-fold). A further increase in humidity level (e.g., from 30% to 50%) yields a smaller additional increase of the response to NO_2 (1.05-fold). Because water vapor is an electron acceptor like NO_2, the further increase of the response for NO_2 at higher RH values can be qualitatively understood.

A comparison between the responses toward 100 ppm of NO_2 for MoS_2/CNT hybrids and pristine va-CNTs operated at room temperature is shown in Figure S6d (Supporting Information). MoS_2/CNTs show higher response and better baseline recovery properties than pristine va-CNTs. It is in agreement with previously reported results of better performance of MoS_2 over carbon-based materials when used as a chemical sensor.[28,29] Additionally, the performance of MoS_2/CNTs is superior to that of pristine va-CNTs in humidity conditions (Figure S6e, Supporting Information), where the response slightly decreases in the presence of humidity (Figure S6e, Supporting Information). It can be derived that the MoS_2/CNT system is more suitable for detecting NO_2 under real conditions in which ambient humidity is present. It should be noted that the conductive measurements were performed with top contacts (Ag) where the MoS_2 HNPs are situated (Figure S5b,c, Supporting Information). This top contact geometry (Figure 9) implies that a significant part of the current measured between the contacts actually flows through the MoS_2 HNP layer. However, the response to NO_2 can be attributed to the hybrid MoS_2 HNPs-CNT film because; (1) the CNTs act as a support to MoS_2 HNPs and, (2) increases the accessibility of NO_2 molecules to reach the exposed edges of MoS_2 HNPs where they adsorb. To the best of our knowledge, a successful detection of 25 ppb of NO_2 employing MoS_2 has never been reported previously. The MoS_2/CNT hybrid material exhibits a much larger detection range as compared to the previously reported sensor

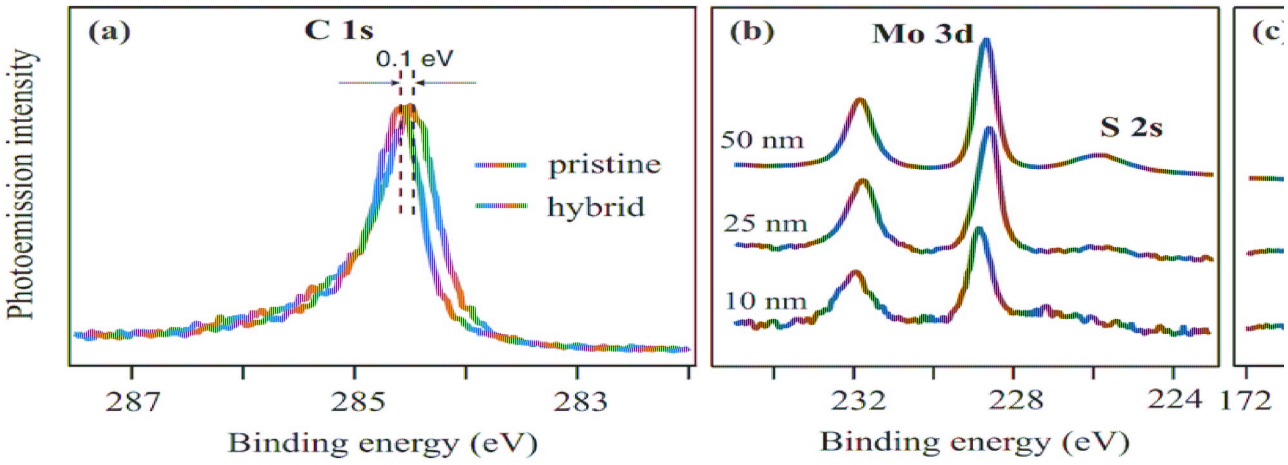

Figure 5. XPS spectra: Binding energy (eV) versus photoemission intensity (arbitrary unit) plots for the MoS_2/CNT samples. a) The C1s core level spectra for pristine CNT sample and for 25 nm Mo film on CNT sulfurized sample. b,c) The core level spectra for Mo 3d, S 2p from three samples with initial Mo film thickness 10, 50, and 300 nm on CNT sulfurized.

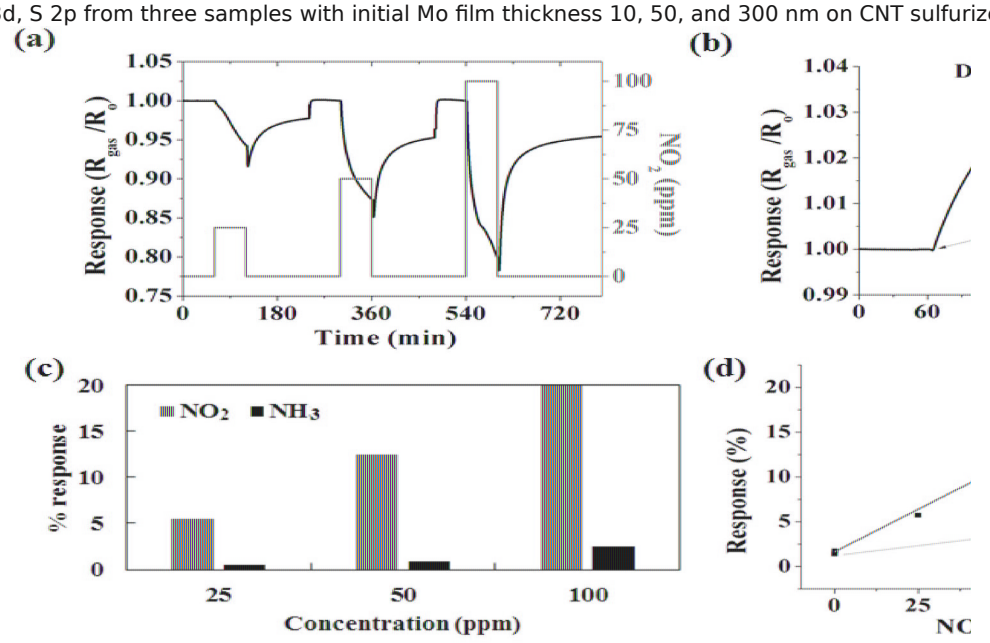

Figure 6. a) The MoS_2/CNT sensor response as a function of three nitrogen dioxide concentrations (25, 50, and 100 ppm) when operated at room temperature. Mild heating at 100 °C is applied at the beginning of the recovery phase to accelerate this process. b) Resistance change of MoS_2/CNT sensor when exposed to NH_3 vapors at 100 and 50 ppm. c) Comparison of the responsiveness toward NO_2 and NH_3 at 25, 50, and 100 ppm. d) Calibration curve for the response toward NO_2 the inset shows an enlargement of the low concentration area of the curve.

results for MoS_2 or carbon-based semiconducting materials (monolayer,[7] multilayer,[30] or vertically aligned[3] MoS_2 (0.3 to 0.8 ppm and 0.1 to 100 ppm, respectively), pristine and/or functionalized va-CNT (0.5 ppm),[31] and MoS_2 and graphene hybrid (50 ppb).[32] The most common gas-sensing principle relies on the adsorption and desorption of gas molecules on sensing materials. Therefore, it is quite understandable that by increasing the contact interfaces between the analysts and sensing materials, the sensitivity can be significantly enhanced. The extremely high surface-to-volume ratio and hollow structure of nanomaterials like our MoS_2/CNT hybrid system are ideal for the adsorption of gas molecules.

To reveal the NO_2 gas-sensing properties of our device DFT calculations were performed (see the Experimental Section). Since the pristine va-CNT system has lower sensitivity[31] (Figure S6, Supporting Information) compared to our MoS_2/CNT system and considering the gas-sensing measurement geometry (Figure 9) we focus on the effect of the MoS_2 HNPs with exposed edges (Figure 3b), which might play a dominant role in the sensing mechanism. For modeling the MoS_2 HNPs edge sites, we applied a MoS_2 multilayer ribbon geometry having an infinite length in the *x* and *z* directions by using periodic boundary conditions and finite width of six Mo atoms in the *y* direction (**Figure 8**). Since the MoS_2 HNPs are much larger (200–300 nm) in the *y* direction, we performed convergence test with respect to

the ribbon width. We found that six Mo atoms width in the *y* direction is sufficiently large to obtain converged values of the NO_2 adsorption energy. The experimentally observed 2H stacking of the MoS_2 causes that the edge type of the multilayer ribbon alternate in the *z*-direction between the so-called Mo edge and S edge on each side (Figure 8). In our calculations Mo edges are saturated with S dimers according to experimental and theoretical findings.[33,34] As a first step, we investigated the electronic properties of the system without

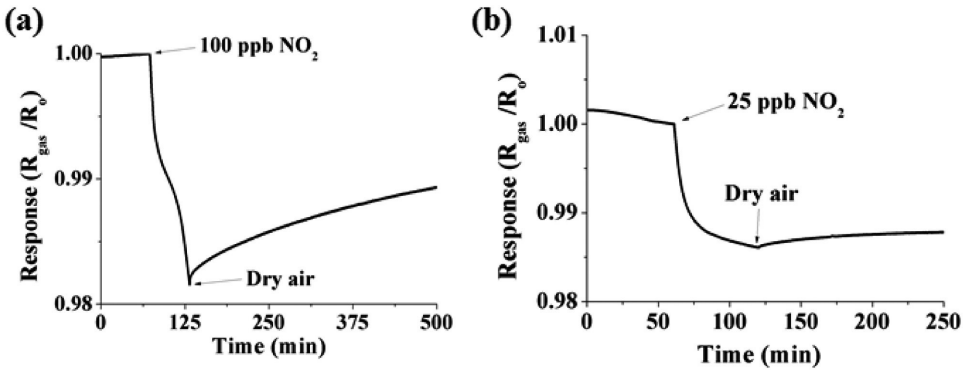

Figure 7. Responses at room temperature of NO_2 of MoS_2/CNT sensor. a) 100 ppb and b) 25 ppb.

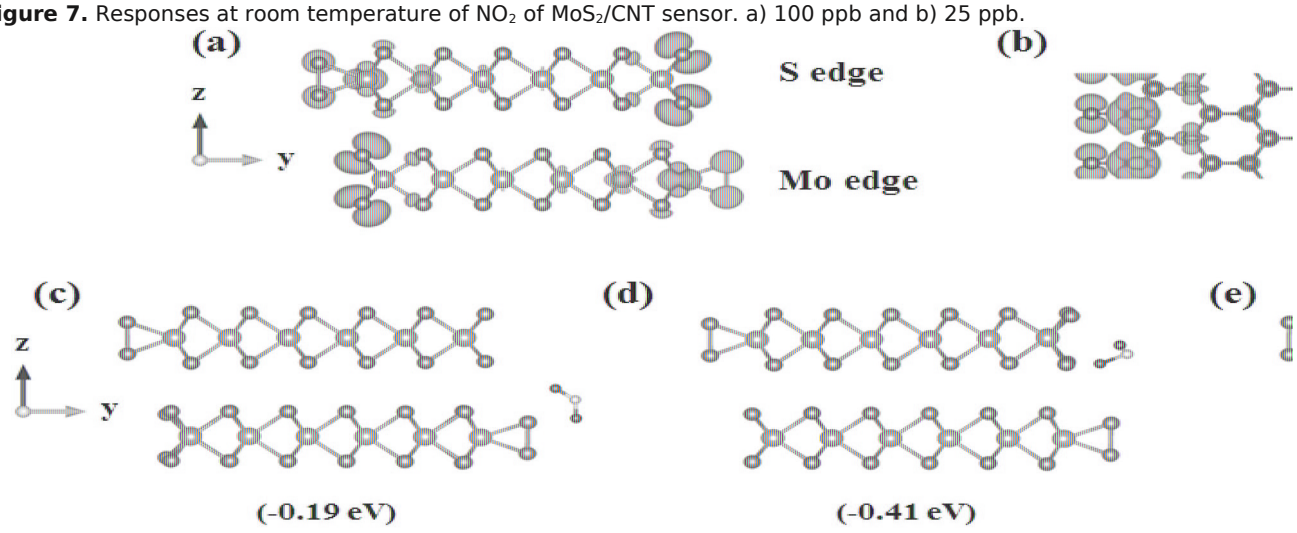

Figure 8. a–b) Charge density plots around the Fermi-level of the modeled MoS_2 HNP unit cell. The isovalue is set to be $10^{-3}e$ Å^{-3} in both the *zy* and the *xy* planes. The metallic edge states localized at the Mo edges and S edges is clearly seen. c–e) Side views (*zy*) of the most favorable adsorption configurations for NO_2 at the edges. The low adsorption energy at the Mo edge (c) compared to the S edge configurations (d) and (e) is originated from the S dimer passivation of the Mo edge. Purple, red, orange, and white spheres represent molybdenum, oxygen, sulfur, and nitrogen, respectively.

gas molecules. Figure 8a,b shows the charge density distribution near the Fermi level where charge localization can be seen along the edges. These unusual metallic edge states were predicted earlier in MoS_2[33] and also measured both in singlelayer[33] and multilayer[35] MoS_2 samples by using scanning tunneling microscopy. Because the states in the inner part of the multilayer ribbon are essentially bulk-like with a finite band gap, we assume that the current mainly flows around the edges in the *x*,*y*- and *z*-directions for our MoS_2 HNPs.[33] We have experimentally observed relatively low sensor resistance (a few Ohms for MoS_2/CNT while a few hundreds of Ohms for pristine CNT samples), for a semiconductor MoS_2 material supports these arguments. Next, we computed the adsorption energies of the NO_2 molecule at the different edges (Mo edge and S edge). The relaxed geometries with one Mo edge and two S edge configurations are shown in Figure 8b–d. In the S edge case, we investigated two geometries where the NO_2 is situated in the *xy* (Figure 8c) and the *yz* (Figure 8d) plane. In the latter case, the interaction between the underlying MoS_2 layers is more significant. The adsorption energies of the different positions of the NO_2 gas molecule were evaluated using $E_a = E_{(MoS_2 - NO)_2} - \square\square E_{(MoS_2)} + E_{(NO_2)} \square\square$, where $E_{(MoS_2 - NO_2)}$ is the total energy of the optimized structure of NO_2 adsorbed on MoS_2, $E_{(MoS_2)}$ is the total energy of the pristine MoS_2, and $E_{(NO)_2}$ is the energy of the isolated gas molecule. In the Mo edge and two S edge configurations, the adsorption energies are −0.19, −0.41, and −0.51 eV, respectively. For comparison, we also calculated the adsorption energy when NO_2 is adsorbed onto the surface (basal plane) of a multilayer MoS_2 sample, which was found −0.13 eV similar to the case of the monolayer MoS_2.[10] We note that this tendency of the adsorption energies of NO_2 where the molecule adsorbed more likely at the edges, especially the S edge, was previously reported for monolayer MoS_2 edge calculations.[3] The moderate values of the adsorption energies can be considered as physisorption rather than chemisorption, especially in the case of the saturated Mo edge.[4] Our experimental findings where the complete baseline recovery was achieved after just 100 °C annealing (Figure 6a) are in qualitative agreement with the DFT results. Finally, Bader analysis[36] is performed to predict the charge transfer between the MoS_2 and NO_2. It is found that in all geometries NO_2 behaves as an electron acceptor and the values of the charge transfer are 0.18*e*, 0.59*e*, and 0.48*e* for the different attachments. These values are larger compared to the case when NO_2 adsorbed on the basal plane (0.1*e*)[7,9] highlighting the increased p-doping when NO_2 adsorbed on the

edges. Therefore, our DFT calculations revealed that the NO_2 molecules are not only likely to be adsorbed onto the edges of MoS_2 HNPs, but also increase the p-doping compared to the case of the MoS_2 basal plane adsorption. Because in our measurements, the gas sensing is based on the resistivity of the sample, the increased p-doping at the edges of the MoS_2 HNPs, where the current flows, explains the enhanced sensitivity of our MoS_2/CNT hybrid material.

2.3. Gas-Sensing Mechanism

It is well-known that NO_2 acts as an electron acceptor while NH_3 acts as an electron donor in the case of MoS_2 and CNT.[37]
Our results show a clearly enhanced response of the MoS_2/ CNT system to both NO_2 and NH_3 in which the resistance of the device decreases with NO_2 adsorption and increases with the adsorption of NH_3. Single-layer MoS_2 samples behave usually as n-type semiconductors.[38,39] However, the n-type or p-type character of MoS_2 depends on its morphology, the nanostructure alignment on the substrate.[3] It has been also reported,[40] that n-type and p-type regions can coexist on the same substrate. Furthermore, vertically aligned MoS_2 layers with exposed edges (a similar morphology as the one reported here) have been found to behave as p-type.[3] Also, MoS_2 thin films grown on graphene show p-type behavior.[15] Based on this, we consider our MoS_2/CNT hybrid structure as a p-type semiconductor material similar as previously reported for MoS_2/graphene hybrid systems[15,32] and in agreement with our experimental findings.

The mechanism of gas sensing in MoS_2/CNT is twofold (**Figure 9**). NO_2 molecules can adsorb on the edges and on the surface of MoS_2 HNPs where electronic charge transfer occurs from the MoS_2 HNP toward the molecule. This mechanism creates an accumulation region of holes and a consequent resistance decrease in the hybrid film. In Figure 6a slow and fast response (recovery) can be seen, which might correspond to the adsorption on the edge sites and on the surface, respectively.[28] According to the response signal, we suppose that the edges play a major role, however surface adsorption also helps to achieve the outstanding sensitivity. Additionally, NO_2 molecules can also interact and adsorb onto the CNT outer wall resulting in further increasing the p-doping of the hybrid film.[37,41] This translates again in the MoS_2/CNT hybrid film lowering its resistance. Nevertheless, future study to understand the detailed adsorption mechanism(s) is necessary.

A way often employed for ameliorating CNT gas sensors performance consists of functionalizing CNTs with metal clusters.[6,31,42] It is well known that CNTs decorated with gold nanoparticles improve their response toward NO_2.[31] The CNTs decoration with Au nanoparticles results in the p-doping of CNT films showing a response of 2% to 500 ppb of NO_2.[41] As discussed above, similarly to the Au functionalization yet achieving a significantly higher response, the MoS_2 layer on top of va-CNTs has also a strong p-doping effect on the hybrid CNT film (e.g., the response is 1.4% to a much lower NO_2 concentration of 25 ppb).

According to the theoretical and experimental findings, both the MoS_2 HNPs with exposed edges and the va-CNT layer play an important role in the observed sensitivity. Since the MoS_2 HNPs are on top of the va-CNT forest, the accessibility for the gas molecules to the exposed HNP edges is significantly increased (Figure 9). In our MoS_2/CNT hybrid material, NO_2 molecules can attach to the MoS_2 edges from all directions compared to the case where the sensing material (MoS_2) is grown on a flat substrate. In addition, the va-CNTs not only act as a support for the MoS_2 HNPs, but they are also sensitive to adsorption of gas molecules. Therefore, the enhanced NO_2 sensitivity of our device over pristine CNTs is assigned to the MoS_2/CNT hybrid system.

3. Conclusions

Abundant MoS_2 HNPs were grown on the va-CNT template layer by using a simple CVD technique. The CNT template layer plays an important role in the growth of hexagonal MoS_2. The high quality and crystallinity MoS_2 of HNPs were confirmed by using Raman, XPS, NEXAFS, and TEM characterization techniques. The HNPs with a thickness about 20 nm and a length of several hundreds of nanometers with highly exposed edges were produced by controlling the initial Mo film thickness. The MoS_2/CNT shows an enhanced room temperature gas-sensing performance as compared to monolayer MoS_2 or pristine CNTs. It also shows gas-sensing properties to both low and high (a few ppb to a few hundreds of ppm) concentrations of NO_2. Mild heating is necessary for desorbing NO_2 from the surface and completely recovering baseline resistance in a few minutes. The excellent NO_2 sensing response of the MoS_2/CNT hybrid system comes from the large affinity of NO_2 for MoS_2 HNPs edges and the more significant charge transfer at the edges, as revealed by DFT calculations. For gas-sensing application, it provides an enhanced surface area for the gas-adsorption and additional access-gate for the NO_2 to reach the HNPs provided by the underneath CNT forest. The current result could be beneficial for future gas-sensing studies to improve further the response and detection limit.

4. Experimental Section

Material Growth: A two-step strategy: (1) growth of va-CNTs and (2) sulfurization of Mo film deposited on it was used to produce MoS_2 HNPs on CNT (MoS_2/CNT) hybrid material. The growth of va-CNTs (with a typical height of 350 μm) on an Si substrate (with 10 nm Fe catalyst layer on it) was carried out as explained in detail elsewhere.[31] The as-synthesized va-CNTs[31] were used as a template substrate for hexagonal MoS_2 nanoplates growth. A sputter-coated Mo film (10–50 nm) deposited using Quorum system on the CNT samples was used as a starting material. The S powder (99.5%), purchased from Alfa Aesar was used without any further purification. The Mo film samples were set downstream to the Ar (purity 99.9995%) flow at a distance of about 2 cm from the S source. The quartz tube was first flushed for 1 h to remove oxygen using a 0.725 L min^{-1} Ar flow. Subsequently, the Mo/CNT samples were subjected to double sulfurization at 850 °C for 30 min each, under constant Ar flow (0.725 L min^{-1}) at atmospheric

pressure. Afterward, the furnace was cooled down naturally to room temperature. The HNP growth parameters such as substrate temperature (850 °C), Ar gas flow (0.725 L min^{-1}), S powder quantity (210 mg for each sulfurization), and synthesis duration (60 min) were adapted from the previously reported MoS_2 nanosheet growth technique.[20]

Material Characterization Techniques: The sulfurized Mo films on va-CNTs samples morphology was characterized using a field-emission scanning electron microscope Hitachi 2000 and FEI Helios NanoLab 650 were used. The structural characterization was performed by employing an aberration-corrected TEM (FEI Titan Low-Base), working at 200 kV equipped with a Cs probe corrector, a high angle annular dark field imaging detector for imaging and energy dispersive spectroscopy (EDS) spectrometer. The specimens for TEM observations were prepared by spreading a few drops of a solution (some material removed from the sample and dissolved in isopropyl alcohol) on a lacey-carbon-coated copper grid. Raman spectroscopy was performed using a Horiba microRaman confocal microscopic system (Lab-RAM) with 483 nm laser. NEXAFS and XPS measurements were performed using synchrotron radiation from Russian–German Beamline at BESSY II, HelmholtzZentrum Berlin, Germany. The C K-edge spectra were obtained using the sample drain current mode. Photoemission spectra were acquired with a hemispherical Phoibos 150 electron energy analyzer (SPECS GmbH) for high-energy-resolution photoemission experiments. XPS measurements were carried out in the normal emission geometry. All the measurements were carried out at room temperature. Photoemission spectra obtained were fitted using Gaussian–Lorentzian convolution functions with a simultaneous background optimization.

Sensor Device Fabrication and Characterizations: To fabricate the sensor device, the MoS_2/CNT hybrid samples were processed as follows. Twowire contacts were made on the surface (on MoS_2 HNP) of samples by employing a silver paste (Ag component metallization, Heraeus) and Pt wires. Samples were glued with a thermally conductive epoxy to an alumina heating plate and wire-bonded to a printed circuit board (Figure S5b,c, Supporting Information), which can be connected inside a 35 mL test chamber (Figure S5d, Supporting Information). This chamber was connected to a fully automated, continuous flow measurement set-up in which reproducible concentrations of dry or humidified gas mixtures could be delivered by mass-flow controllers.

The MoS_2/CNT sensors were tested with different gases at room temperature (20 °C). In a typical measurement process, the total flow was adjusted to 100 mL min^{-1}. Initially, samples were in a dry air flow for 1 h to stabilize their baseline resistance. Then, the samples were exposed to a given concentration of NO_2 or NH_3 diluted in the air for 1 h (in Figure S5a of the Supporting Information, a table for typical sensing experimental conditions are provided), and the evolution of their room-temperature resistance was monitored employing an Agilent 34972A multimeter. These measurements were spanned for over one month without noticeable changes in response and sensitivity. Some of the sensing measurements were also repeated after keeping the sample in air for one month and reproducible results were observed. Calibrated gas cylinders in which either nitrogen dioxide (at 1 or 100 ppm) or ammonia (at 100 ppm) balanced in the dry synthetic air. During the ppb range measurements, one of these cylinders was connected to an automated gas dilution system that comprised a cylinder of a dry synthetic air and two mass-flow controllers. Employing this system, the original concentration in the calibrated cylinders could be further reduced by a factor of up to 50. For example, by adjusting the dilution factor to 40, one could deliver 25 ppb of NO_2 when the 1 ppm NO_2 bottle was used. Finally, the samples were cleaned in a dry air. In some cases, the process of cleaning comprised two steps. In the first step, the samples were heated to 100 °C for 2 h by using the heating plate. In the second step, the heating was switched off and samples were flown with dry air for 1 h at room temperature. After this cycle, the samples were ready for another measurement cycle.

For the effect of humidity measurements in gas sensing was investigated, the baseline resistance of the samples was stabilized at a given level of humidity (e.g., 30% RH at 20 °C). This humidity level was kept constant during the exposure to NO_2 or NH_3.

Computational Details: All calculations were performed in the framework of spin-polarized DFT theory by using the Vienna ab initio simulation package.[43] Exchange–correlation effects were taken into account in the framework of the generalized gradient approximation by the Perdew–Burke–Ernzerhof functional.[44] Projector augmented wave pseudopotentials[45] were used, and the kinetic energy cut-off for the plane wave expansion was 400 eV. The geometry of the atomic positions was relaxed using the conjugate-gradient method until the forces of the atoms were reduced to 0.02 eV $Å^{-1}$, and the Brillouin-zone was sampled using a 6 × 1 × 4 Monkhorst–Pack mesh. Large vacuum distance in the y direction (i.e., more than 13 Å) was imposed in the model to avoid unwanted interactions between the edges. The dimensions of the rectangular supercell were 6.36, 30.2, and 12.4 Å in the *x*, *y*, and *z* direction, respectively.

Supporting Information

Supporting Information is available from the Wiley Online Library or from the author.

Acknowledgements

This research used resources of the Electron Microscopy facilities of Masdar Institute and University of Mons. This research leading to these results received funding in part from European Union Seventh Framework H2020 Program under Grant Agreement No. 696656 Graphene Flagship. J.-F.C. is Senior Research Associate of FRS-FNRS. R.A. gratefully acknowledges the support from the Spanish Ministerio de Economia y Competitividad (MAT2016-79776-P), from the Government of Aragon and the European Social Fund under the project "Construyendo Europa desde Aragon" 2014–2020 (Grant No. E/26), and from the European Union H2020 program ETN project "Enabling Excellence" Grant Agreement No. 642742. E.L. was supported by the Catalan Institution for Research and Advanced Studies via the ICREA Academia Award and MINECO-FEDER (grant no. TEC2015-71663-R) and J.C.-C. was supported by Universitat Rovira i Virgili via a Martí i Franquès predoctoral fellowship. This research used resources of the "Plateforme Technologique de Calcul Intensif (PTCI)," which was supported by the F.R.S.-FNRS under Convention No. 2.5020.11. This work was supported by the Helmholtz-Zentrum Berlin für Materialien und Energie within a bilateral Russian–German Laboratory program. A.A.M. acknowledges support from DFG, Grant No. LA655/132. D.V.V. acknowledges Saint Petersburg State University (SPbU) for research Grant No. 15.61.202.2015.

Conflict of Interest
The authors declare no conflict of interest.

Keywords
CNT, DFT calculations, gas sensor, MoS_2, nanoplates

[1] G. Korotcenkov, *Mater. Sci. Eng. B* **2007**, *139*, 1.
[2] T. Zhang, S. Mubeen, N. V. Myung, M. A. Deshusses, *Nanotechnology* **2008**, *19*, 332001.
[3] S. Y. Cho, S. J. Kim, Y. Lee, J. S. Kim, W. B. Jung, H. W. Yoo, J. Kim, H. T. Jung, *ACS Nano* **2015**, *9*, 9314.
[4] S. J. Ray, *Sens. Actuators, B* **2016**, *222*, 492.
[5] J. Kong, N. R. Franklin, C. Zhou, M. G. Chapline, S. Peng, K. Cho, H. Dai, *Science* **2000**, *287*, 622.
[6] P. Young, Y. Lu, R. Terrill, J. Li, *J. Nanosci. Nanotechnol.* **2005**, *5*, 1509.
[7] D. J. Late, Y. K. Huang, B. Liu, J. Acharya, S. N. Shirodkar, J. Luo, A. Yan, D. Charles, U. V. Waghmare, V. P. Dravid, C. N. Rao, *ACS Nano* **2013**, *7*, 4879.
[8] B. Cho, M. G. Hahm, M. Choi, J. Yoon, A. R. Kim, Y.-J. Lee, S.-G. Park, J.-D. Kwon, C. S. Kim, M. Song, Y. Jeong, K.-S. Nam, S. Lee, T. J. Yoo, C. G. Kang, B. H. Lee, H. C. Ko, P. M. Ajayan,
D.-H. Kim, *Sci. Rep.* **2015**, *5*, 8052.
[9] Q. Yue, Z. Shao, S. Chang, J. Li, *Nanoscale Res. Lett.* **2013**, *8*, 425.
[10] S. Zhao, J. Xue, W. Kang, *Chem. Phys. Lett.* **2014**, *595*, 35.
[11] S. Tongay, J. Suh, C. Ataca, W. Fan, A. Luce, J. S. Kang, J. Liu, C. Ko, R. Raghunathanan, J. Zhou, F. Ogletree, J. Li, J. C. Grossman, J. Wu, *Sci. Rep.* **2013**, *3*, 2657.
[12] H. Nan, Z. Wang, W. Wang, Z. Liang, Y. Lu, Q. Chen, D. He, P. Tan, F. Miao, X. Wang, J. Wang, Z. Ni, *ACS Nano* **2014**, *8*, 5738.
[13] Y. H. Kim, K. Y. Kim, Y. R. Choi, Y.-S. Shim, J.-M. Jeon, J.-H. Lee, S. Y. Kim, S. Han, H. W. Jang, *J. Mater. Chem. A* **2016**, *4*, 6070.
[14] S. J. Ray, M. V. Kamalakar, R. Chowdhury, *J. Phys.: Condens. Matter* **2016**, *28*, 195302.
[15] Q. He, Z. Zeng, Z. Yin, H. Li, S. Wu, X. Huang, H. Zhang, *Small* **2012**, *8*, 2994.
[16] Y. Shi, H. Li, L. J. Li, *Chem. Soc. Rev.* **2014**, *44*, 2744.
[17] G. Deokar, D. Vignaud, R. Arenal, P. Louette, J. F. Colomer, *Nanotechnology* **2016**, *27*, 075604.
[18] H. Dong, C. Liu, H. Ye, L. Hu, B. Fugetsu, W. Dai, Y. Cao, X. Qi, H. Lu, X. Zhang, *Sci. Rep.* **2015**, *5*, 17542.
[19] H. Yoo, A. P. Tiwari, J. Lee, D. Kim, J. H. Park, H. Lee, *Nanoscale* **2015**, *7*, 3404.
[20] G. Deokar, N. S. Rajput, P. Vancso, F. Ravaux, M. Jouiad, D. Vignaud, F. Cecchet, J. F. Colomer, *Nanoscale* **2017**, *9*, 277.
[21] S. Han, C. Yuan, X. Luo, Y. Cao, T. Yu, Y. Yang, Q. Li, S. Ye, *RSC Adv.* **2015**, *5*, 68283.
[22] M. Remskar, A. Mrzel, Z. Skraba, A. Jesih, M. Ceh, J. Demsar, P. Stadelmann, F. Levy, D. Mihailovic, *Science* **2001**, *292*, 479.
[23] Z. Wu, D. Wang, X. Liang, A. Sun, *J. Cryst. Growth* **2010**, *312*, 1973.
[24] Y. Shi, W. Zhou, A.-Y. Lu, W. Fang, Y.-H. Lee, A. L. Hsu, S. M. Kim, K. K. Kim, H. Y. Yang, L.-J. Li, J.-C. Idrobo, J. Kong, *Nano Lett.* **2012**, *12*, 2784.
[25] L. Cai, J. He, Q. Liu, T. Yao, L. Chen, W. Yan, F. Hu, Y. Jiang, Y. Zhao, T. Hu, Z. Sun, S. Wei, *J. Am. Chem. Soc.* **2015**, *137*, 2622.
[26] G. Pagona, C. Bittencourt, R. Arenal, N. Tagmatarchis, *Chem. Commun.* **2015**, *51*, 12950.
[27] C. Lee, H. Yan, L. E. Brus, T. F. Heinz, J. Hone, S. Ryu, *ACS Nano* **2010**, *4*, 2695.
[28] A. L. Friedman, F. K. Perkins, A. T. Hanbicki, J. C. Culbertson, P. M. Campbell, *Nanoscale* **2016**, *8*, 11445.
[29] A. L. Friedman, F. Keith Perkins, E. Cobas, G. G. Jernigan, P. M. Campbell, A. T. Hanbicki, B. T. Jonker, *Solid-State Electron.* **2014**, *101*, 2.
[30] H. Long, L. Chan, A. Harley-Trochimczyk, L. E. Luna, Z. Tang, T. Shi, A. Zettl, C. Carraro, M. A. Worsley, R. Maboudian, *Adv. Mater. Interfaces* **2017**, *4*, 1700217.
[31] P. R. Mudimela, M. Scardamaglia, O. Gonzalez-Leon, N. Reckinger, R. Snyders, E. Llobet, C. Bittencourt, J. F. Colomer, *Beilstein J. Nanotechnol.* **2014**, *5*, 910.
[32] H. Long, A. Harley-Trochimczyk, T. Pham, Z. Tang, T. Shi, A. Zettl, C. Carraro, M. A. Worsley, R. Maboudian, *Adv. Funct. Mater.* **2016**, *26*, 5158.
[33] M. V. Bollinger, J. V. Lauritsen, K. W. Jacobsen, J. K. Norskov, S. Helveg, F. Besenbacher, *Phys. Rev. Lett.* **2001**, *87*, 196803.
[34] J. V. Lauritsen, J. Kibsgaard, S. Helveg, H. Topsoe, B. S. Clausen,
E. Laegsgaard, F. Besenbacher, *Nat. Nanotechnol.* **2007**, *2*, 53.
[35] A. A. Koós, P. Vancsó, G. Z. Magda, Z. Osváth, K. Kertész, G. Dobrik, C. Hwang, L. Tapasztó, L. P. Biró, *Carbon* **2016**, *105*, 408.
[36] G. Henkelman, A. Arnaldsson, H. Jónsson, *Comput. Mater. Sci.* **2006**, *36*, 354.
[37] R. Ionescu, E. H. Espinosa, E. Sotter, E. Llobet, X. Vilanova,
X. Correig, A. Felten, C. Bittencourt, G. V. Lier, J. C. Charlier, J. J. Pireaux, *Sens. Actuators, B* **2006**, *113*, 36.
[38] B. Radisavljevic, A. Radenovic, J. Brivio, V. Giacometti, A. Kis, *Nat. Nanotechnol.* **2011**, *6*, 147.
[39] K. S. Novoselov, D. Jiang, F. Schedin, T. J. Booth, V. V. Khotkevich, S. V. Morozov, A. K. Geim, *Proc. Natl. Acad. Sci. USA* **2005**, *102*, 10451.
[40] S. McDonnell, R. Addou, C. Buie, R. M. Wallace, C. L. Hinkle, *ACS Nano* **2014**, *8*, 2880.
[41] Z. Zanolli, R. Leghrib, A. Felten, J. J. Pireaux, E. Llobet, J. C. Charlier, *ACS Nano* **2011**, *5*, 4592.
[42] A. Star, V. Joshi, S. Skarupo, D. Thomas, J.-C. P. Gabriel, *J. Phys.*
Chem. B **2006**, *110*, 21014.
[43] G. Kresse, J. Hafner, *Phys. Rev. B* **1994**, *49*, 14251.
[44] J. P. Perdew, K. Burke, M. Ernzerhof, *Phys. Rev. Lett.* **1996**, *77*, 3865. [45] P. E. Blöchl, *Phys. Rev. B* **1994**, *50*, 17953.